Available online at www.sciencedirect.com
ScienceDirect
Journal of the European Ceramic Society 27 (2007) 3365–3370
www.elsevier.com/locate/jeurceramsoc

Pore channel closure in sintering of a ring of three spheres

Fumihiro Wakai [a,*], Diego Gómez-Garcia [b], Arturo Domínguez-Rodríguez [b]

[a] *Secure Materials Center, Materials and Structures Laboratory, Tokyo Institute of Technology, R3-23, 4259 Nagatsuta, Midori, Yokohama 226-8503, Japan*
[b] *Departmento de Fisíca de la Materia Condensada, Universidad de Sevilla, Aptdo. 1065, 41080 Sevilla, Spain*

Available online 16 April 2007

Abstract

Three-dimensional numerical simulation of sintering of a ring of three spheres was performed to investigate the effect of the ratio of grain boundary energy γ_{gb} to surface energy γ_s, or dihedral angle, to the nature of pore channel closure. As the ring shrank, the hole at the center closed to form a triple junction. The force acting between particles, that was the sintering force, was defined by including both surface tension and grain boundary tension. The shrinkage rate was approximately proportional to the sintering force, but became non-linear at lower γ_{gb}/γ_s. The sintering force, and also, shrinkage rate increased with decreasing γ_{gb}/γ_s, then, the hole closed in a short time at low γ_{gb}/γ_s.

Keywords: Sintering; Micromechanical modeling

1. Introduction

Sintering is a thermal process that transforms a powder compact into a bulk material, and it is used for mass production of complex-shaped components. The powder particles and pore channel networks change their shapes through diffusion,[1] which is driven by the difference in curvature-dependent chemical potential. Sintering is a complicated process of microstructural evolution involving bond formation, neck growth, pore channel closure, pore shrinkage, densification, coarsening, and grain growth. But the elementary processes of sintering can be essentially described by using some particle clusters. The Frenkel[2]–Kuczynski[3] model, that is the sintering of two identical spheres, has been used to study bond formation, neck growth, and interparticle shrinkage. Coble[4] proposed a geometrically simple model for analyzing shrinkage of pore channel assuming a cylindrical pore along the grain edges. This is a valid assumption for sintering of three wires.[5] The uniform pore shrinkage among wires can be represented by a sintering model of three circles in two dimensions, and has been simulated by molecular dynamics,[6] Monte Carlo model,[7] and boundary element method.[8] Due to Rayleigh's surface instability,[9,10] the cylindrical pore channels cannot shrink uniformly when the pore diameter becomes very small. They are disconnected and isolated pores are formed eventually.

On the other hand, pores in an aggregate of sintering spheres are never even approximately cylindrical, because the actual pore channels vary in section and surface curvature.[5] Pore channel closure in three dimensions can be illustrated with Exner's model,[11] that is, sintering of a ring of spheres. The hole at the center shrinks during sintering, and the ring reaches to an equilibrium state where the total energy, i.e., sum of surface energy and grain boundary energy, is minimized. Kellett and Lange[12] determined the thermodynamic requirements for hole closure at the equilibrium. However, three-dimensional sintering simulations are still limited to only the initial stage of sintering before pore closure. For example, Zhou and Derby[13] presented the finite element simulation of the viscous sintering of a ring of three spheres. Maximenko et al.[14] studied shrinkage in the initial stage sintering of a ring of four spheres.

The aim of this paper is to illustrate the whole sintering process of a ring of three spheres until the equilibrium state is attained. We have recently performed the simulation of elementary processes in sintering, and presented a micromechanical model of sintering[15–17]; the shrinkage is described as the motion of the center of mass by the force acting between particles. In the present paper, we further develop the model for various ratios of grain boundary energy γ_{gb} to surface energy γ_s. We show that the relationship between shrinkage rate and driving force becomes non-linear as γ_{gb}/γ_s decreases toward zero. We study

* Corresponding author. Tel.: +81 45 924 5361; fax: +81 45 924 5390.
E-mail address: wakai@msl.titech.ac.jp (F. Wakai).

0955-2219/$ – see front matter © 2007 Elsevier Ltd. All rights reserved.
doi:10.1016/j.jeurceramsoc.2007.02.188

the idealized sintering by assuming a simple diffusion mechanism in this paper. The essential results obtained are general, and can easily be applied to various sintering mechanisms.

2. Numerical computation method

2.1. Ideal sintering

The microstructural evolution in sintering is the result of surface motion, grain boundary motion, and rigid body motion. In real sintering, various diffusion mechanisms, i.e., evaporation–condensation, surface diffusion, grain boundary diffusion, and bulk diffusion, take place concurrently. The relative importance of these diffusion mechanisms to sintering varies with the microstructural evolution itself. We consider a simple case of the idealized sintering in the following sections to avoid these complications; we assume that the microstructural evolution is described by the surface motion only

$$\upsilon = M_s\gamma_s(\kappa - \bar{\kappa}) \tag{1}$$

where υ is the normal velocity, γ_s is surface energy and M_s is the surface mobility. The curvature $\kappa = 1/r_1 + 1/r_2$ is defined by two principal curvatures. The average curvature $\bar{\kappa}$ is given by

$$\bar{\kappa} = \frac{1}{A_s}\int_{A_s} \kappa \, dA \tag{2}$$

where A_s is the total surface area. This surface motion conserves the total mass, and describes the sintering by evaporation–condensation.[16]

2.2. Surface Evolver program

The microstructural evolution in ideal sintering was simulated by using Brakke's Surface Evolver program,[18] which could approximate the surface motion, Eq. (1). The outline of the program is described here briefly. Both the surface and the grain boundary are represented as a set of triangular finite elements, or facets. Each facet consists of three edges and three vertices. The surface and the grain boundary have energies proportional to their area. The program evolves the surface toward minimal energy by a gradient descent method. The gradient of energy at a vertex is a force, which is converted to a velocity vector for the motion. The surface motion by Eq. (1) can be approximated by enforcing the constraint on conservation of the total volume of particles. When there is a constraint, the Surface Evolver program automatically calculates the Lagrange multiplier for the constraint. The Lagrange multiplier for a fixed-volume constraint is the pressure, which is identical to $\gamma_s\bar{\kappa}$. The Surface Evolver program had been applied to simulate grain growth,[19] sintering,[15–17] and coarsening.[20] The sintering of a ring of three spheres was simulated by assuming that the surface energy γ_s, the grain boundary energy γ_s, and the surface mobility M_s were isotropic. The ideal sintering of clusters of identical particles is described by introducing the dimensionless time

$$t^* = \frac{\gamma_s M_s t}{r_0^2} \tag{3}$$

where r_0 is the initial particle radius. The definition of the dimensionless time is consistent with the scaling law of sintering by evaporation–condensation.[16]

3. Results and discussions

3.1. Pore channel closure

The elementary process of pore channel closure was analyzed by using a ring of three spheres as shown in Fig. 1. The ring has a hole in the center, and bonds are formed between particles (Fig. 1(a)). The normal velocity of the surface is proportional to $\kappa - \bar{\kappa}$ in this simulation. The sign of curvature is chosen so that a concave neck has a positive curvature, and a spherical particle has a negative curvature. The direction of the positive velocity vector is outward on the surface of the particle. The outward surface motion expands the neck radius rapidly in the initial stage of sintering (Fig. 1(b)). As three circular grain boundaries grow, the hole radius decreases (Fig. 1(c)). The curvature near the hole increases as the hole shrinks, and the surface velocity toward the hole center is accelerated. Then, the grain boundaries are distorted from circles (Fig. 1(c), lower part). After the hole closes, a triple junction, where three grain boundaries meet, is created in Fig. 1(d). The length of triple junction increases with time as shown in Fig. 1(e).

3.2. Energy reduction

The total energy of the ring is the sum of energies associated with the surface area A_s and the grain boundary area A_{gb}

$$E = \gamma_s A_s + \gamma_{gb} A_{gb} \tag{4}$$

The sintering process depends on the dihedral angle Ψ, which is determined by

$$\gamma_{gb} = 2\gamma_s \cos\left(\frac{\psi}{2}\right) \tag{5}$$

When $\Psi > 0^\circ$ ($\gamma_{gb}/\gamma_s < 2$), the total energy E of the ring is lower than that of three separated spheres $3E_0$, where $E_0 = \gamma_s 4\pi r_0^2$ is the energy of a single sphere, and r_0 is the radius of the sphere. The normalized reduction of energy is defined as

$$\Delta E^* = \frac{E - 3E_0}{3E_0} \tag{6}$$

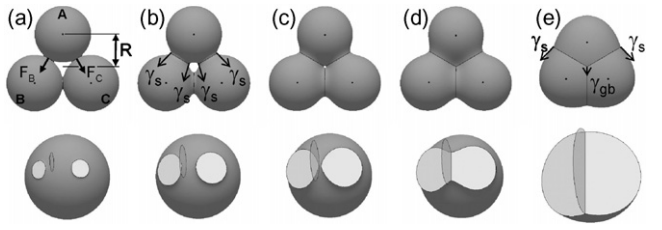

Fig. 1. Sintering of a ring of three spheres. (a) Dimensionless time $t^* = 0.002$, (b) $t^* = 0.013$, (c) $t^* = 0.032$, (d) $t^* = 0.052$ and (e) $t^* = 0.573$ (dihedral angle $\Psi = 151^\circ$, $\gamma_{gb}/\gamma_s = 0.5$). The upper part shows the process of pore channel closure. The lower part shows the formation of a triple junction, where three grain boundaries meet.

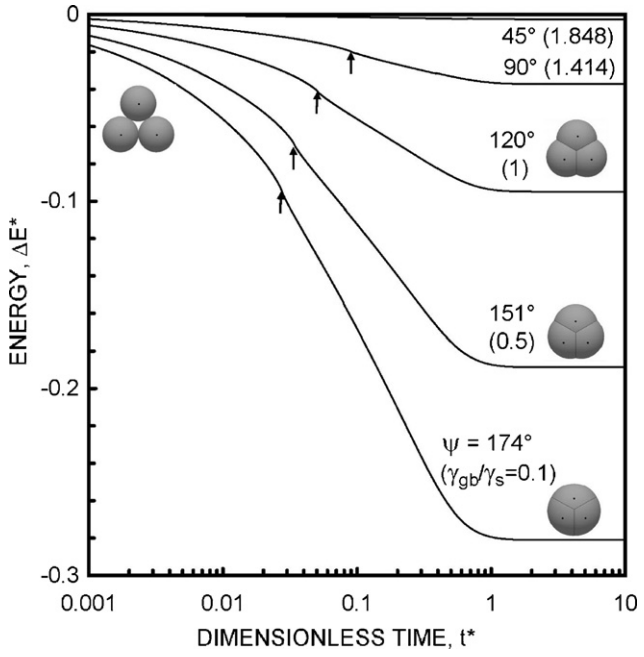

Fig. 2. Normalized reduction in energy as a function of dimensionless time. The equilibrium shapes of clusters with minimal energy are shown. The arrows indicates the pore channel closure.

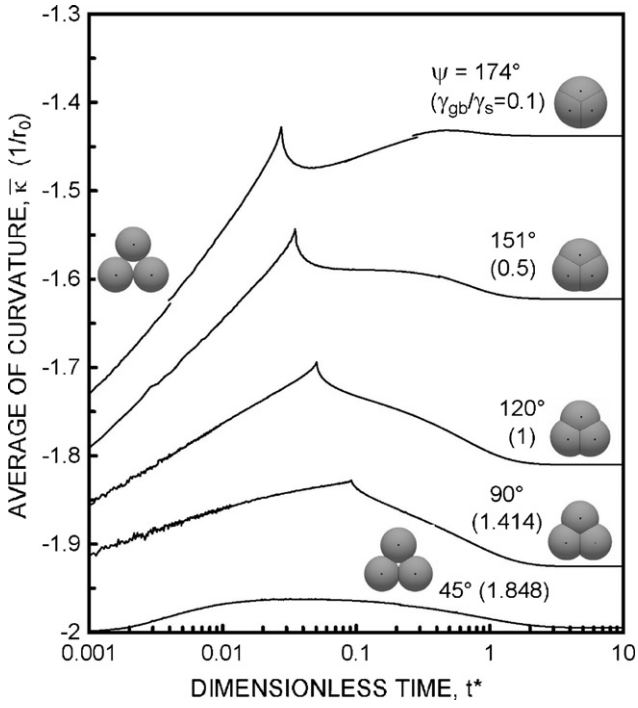

Fig. 3. Average of curvature $\bar{\kappa}$ as a function of dimensionless time. The sharp peaks correspond to the pore channel closure.

The energy reduction in the simulation is plotted as a function of dimensionless time in Fig. 2. The transformation of surface into grain boundary decreases the total energy during sintering. The ring reaches the final equilibrium shape with the minimal energy, which is determined by the dihedral angle, as shown in Fig. 2. The equilibrium energy decreases with decreasing γ_{gb}/γ_s. The particles in equilibrium are partial spheres where the curvature is constant at any position. Kellett and Lange[12] showed that a hole remained in the ring of three spheres at $0 < \Psi < 60^\circ$. The hole disappears at $\Psi > 60^\circ$ ($\gamma_{gb}/\gamma_s < 1.732$). Arrows in Fig. 2 indicates that the pore channel closure takes place during sintering.

3.3. Average of curvature

The surface may have a curvature singularity, where the local curvature diverges to infinity, during topological transitions in sintering, that is, bond formation and pore channel closure. A sphere of radius r_0 has a negative curvature $-2/r_0$. When spheres touch with each other, circular interfaces are created from a singularity at the point of contact. The surface near the neck has a positive curvature. The average of curvature $\bar{\kappa}$, which is defined by Eq. (2), varies with dimensionless time as shown in Fig. 3. $\bar{\kappa}$ increases with time in the initial stage of sintering, because the surface area with positive curvature increases as the neck radius increases. Since both the radius of curvature at the neck[21] and the neck radius[16] are dependent on dihedral angle, the slope of the curve in Fig. 3 increases with dihedral angle

$$\bar{\kappa} + \frac{2}{r_0} \propto 1 - \cos\left(\frac{\psi}{2}\right) \tag{7}$$

The curvature inside the hole diverges to infinity when the hole closes. While curvature at the hole is inversely proportional to the hole radius, the surface area near the hole is proportional to the hole radius. Then, $\bar{\kappa}$ remains finite at the hole closure, and it drops rapidly after the pore channel closure. The curvature reaches to the equilibrium value finally.

3.4. Ring shrinkage

We consider the motion of particles during sintering in Fig. 4, where only two particles are illustrated to show internal structure of the ring. The position of the mass center of a particle can be calculated through a surface integral using the divergence theorem of Gauss.[16] The black dot inside a particle in Fig. 4 indicates the mass center. The distance R from the ring center shifts during sintering because of mass transport from the spherical part to the neck region. Shrinkage of the ring takes place as

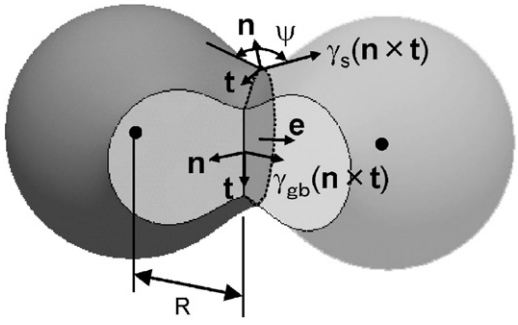

Fig. 4. Geometry of the ring of three spheres after hole closure. Only two particles are illustrated to show internal structure. The black dot inside a particle indicates the mass center.

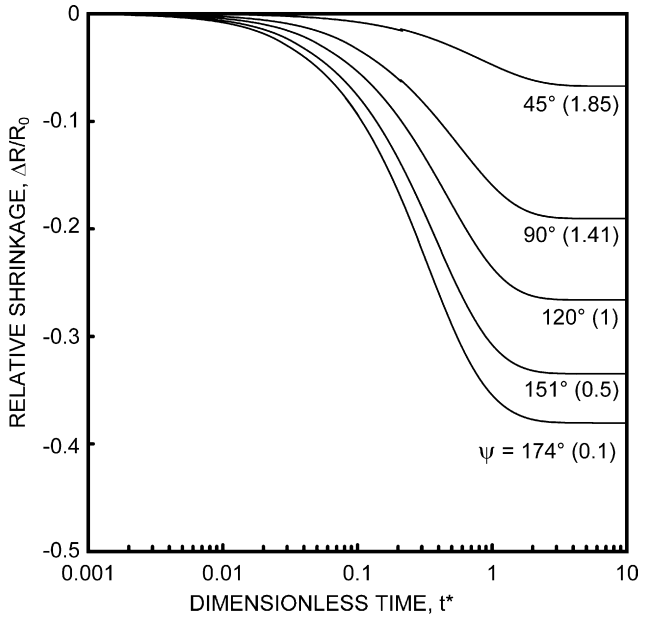

Fig. 5. Motion of particles in sintering of a ring of three spheres. The relative measure of the ring shrinkage is defined by the distance from the ring center.

the mass centers of particles approach to the center. We define a relative measure of the ring shrinkage, or strain

$$\frac{\Delta R}{R_0} = \frac{R - R_0}{R_0} \tag{8}$$

where R_0 is the initial distance from the ring center. Fig. 5 shows that the distance from the center remains initially unchanged. After $t^* = 0.1$, the distance decreases gradually to the final equilibrium value.

The strain rate is calculated from

$$\dot{\varepsilon} = \frac{1}{R_0}\frac{\mathrm{d}R}{\mathrm{d}t^*} \tag{9}$$

and it is plotted in Fig. 6. The strain rate shows a sharp peak at the pore channel closure, and reaches zero at the equilibrium. The shapes of rings at the pore channel closure are shown in Fig. 6 also. The sharp peak is not observed at $\Psi = 45°$, because the pore channel closure does not occur at $\Psi < 60°$. As the dihedral angle increases (or γ_{gb}/γ_s decreases), the peak strain rate increases, then, the time to the pore channel closure becomes shorter.

3.5. Sintering force

The motion of mass centers can be described as a response to the force acting between particles. The sintering force was originally defined by Gregg and Rhines[22] for equilibrium states in which the external force just stops the sintering contraction along one axis of the sinter body. Alternatively, Beere[23] expressed the sintering force as a sum of the pressure acting through the grain boundary area and the surface tension acting between two particles. Beere's idea of sintering force carries over to a non-equilibrium process of sintering. Wakai[17] proposed that the sintering force vector between two particles in Fig. 4 is given by

$$\mathbf{F} = \gamma_s \bar{\kappa} A_{gb}\mathbf{e} + \int_C \gamma_s(\mathbf{n}\times\mathbf{t})\,\mathrm{d}s + \frac{1}{2}\int_L \gamma_{gb}(\mathbf{n}\times\mathbf{t})\,\mathrm{d}s \tag{10}$$

where A_{gb} is the grain boundary area between two particles, $\mathbf{e}$ the unit normal vector to the grain boundary between two particles, $\mathbf{n}$ the unit normal vector to the surface/grain boundary, and $\mathbf{t}$ is the unit tangential vector along the surface triple junction/triple junction. The first term on the right hand side of Eq. (10) arises from the average normal stress, or pressure $\gamma_s\bar{\kappa}$, in the interior of the particle immediately adjacent to the surface. The grain boundary area between two particles in Fig. 4 is bounded by the surface triple junction (dotted line) and the triple junction (solid line). The second term on the right hand side of Eq. (10) is an integration of surface tension along the surface triple junction C. The third term is an integration of grain boundary tension along the triple junction L. The grain boundary tension term is multiplied by 1/2.

The sintering force on a particle is a vector sum of forces acting through grain boundaries with neighbor particles. In the sintering of a ring of three spheres (Fig. 1(a)), the forces $\mathbf{F}_B$ from particle B and $\mathbf{F}_C$ from particle C act on particle A. The net sintering force vector $\mathbf{F}_s = \mathbf{F}_B + \mathbf{F}_C$ points to the hole center. The sintering force increases with time in the initial stage of sintering, and shows a sharp peak at the pore channel closure as shown in Fig. 7. The shapes of grain boundaries at the pore channel closure are also shown in Fig. 7. The maximum sintering force increases with decreasing γ_{gb}/γ_s. The sintering force decreases after the peak, and becomes zero at equilibrium. The decrease in sintering force after the pore channel closure can be understood by comparing Fig. 1(b) and (e). The surface tension 2 γ_s acts on the hole surface in Fig. 1(b). On the other hand, the grain boundary tension γ_{gb} acts along the triple junction after the pore channel closure in Fig. 1(e). The formation of a triple junction decreases the sintering force because $\gamma_{gb} < 2\,\gamma_s$ at $\psi > 0°$.

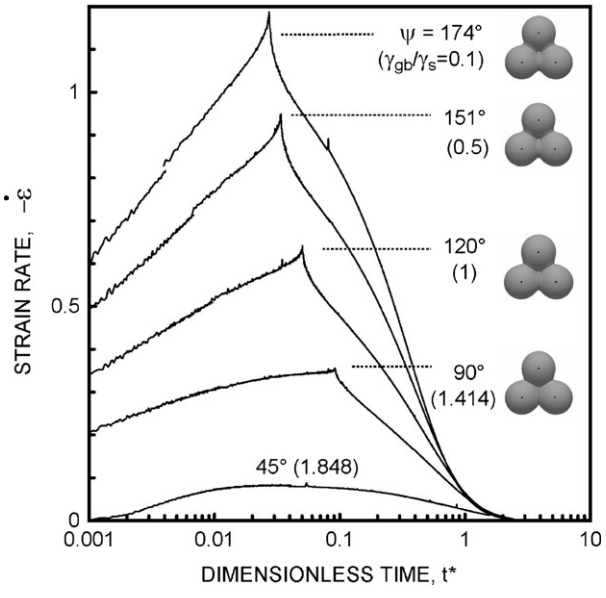

Fig. 6. Strain rate as a function of dimensionless time. The peak shrinkage rate corresponds to the hole closure. The ring shape is shown at the hole closure.

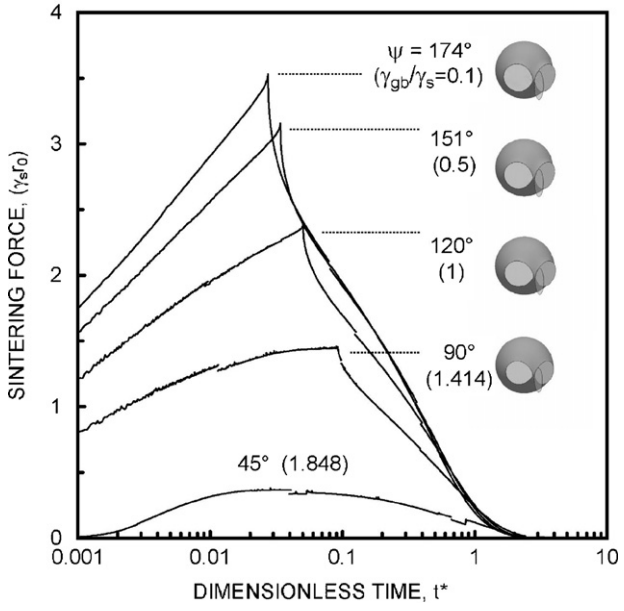

Fig. 7. Sintering force as a function of dimensionless time. The shape of grain boundaries is shown at the peak force.

3.6. Constitutive equation

The relation between the strain rate and the sintering force is plotted in Fig. 8. The strain rate increases with the sintering force linearly before the pore channel closure. The sintering force peaks when the hole closes, then, decreases approximately linearly at $\psi = 45^\circ$ and 90°. The line of $\psi = 45^\circ$ almost overlaps with that of $\psi = 90^\circ$. But, the strain rate–sintering force curves are non-linear at $\psi > 120^\circ$ after the pore channel closure. In viscous sintering[24] and in sintering by "densification mechanism",[25,26] the shrinkage rate is expressed as

$$\dot{\varepsilon} = -\frac{F}{k} \tag{11}$$

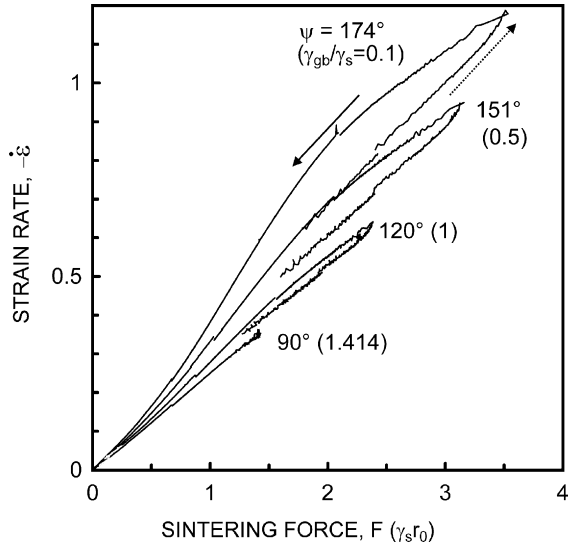

Fig. 8. Relationship betweent he strain rate and the sintering force. The slope of the curve is different before (dotted line) and after (solid line) the peak force.

where k is the effective viscosity. Fig. 8 shows that the motion of the mass center can be approximately described by Eq. (11), even though rigid body motion does not occur. The effective viscosity is given by

$$k = k^* \gamma_s r_0 \tag{12}$$

where k^* is a coefficient. The value of k^* increases with increasing dihedral angle, or decreasing γ_{gb}/γ_s. The strain rate-sintering force curves become non-linear at higher dihedral angles. The slope of the curve is different before (dotted line) and after (solid line) the peak force. The coefficient k^* is not a constant, but varies with time. Since both sintering force and k^* increases with decreasing γ_{gb}/γ_s, the shrinkage rate increases with decreasing γ_{gb}/γ_s as shown in Fig. 6.

The sintering mechanisms of crystalline particles are divided into densifying mechanisms (grain boundary diffusion, lattice diffusion when the grain boundaries act as source/sink of vacancies) and non-densifying mechanisms (surface diffusion, evaporation–condensation, lattice diffusion from/to surface). The rigid body motion of particles takes place in the densifying mechanisms. On the other hand, the non-densifying mechanisms give the shift of mass center of particles but no relative motion of particles. We showed here that the constitutive equation, Eq. (11), is common to densifying processes and also non-densifying processes when we consider the motion of mass center. The constitutive equation is also common to viscous sintering of amorphous particles. The difference in sintering mechanisms affects the effective viscosity k only. Although we showed only the case for evaporation–condensation mechanism, the authors believe that the constitutive equation and also the obtained results on pore channel closure will be a basis for the general theory of sintering.

An unanswered question is the physical origin of the non-linear behavior of the strain rate versus sintering force for higher dihedral angles. In non-equilibrium thermodynamics a generalized displacement is a linear function of a generalized force as long as the deviation from the equilibrium is small. The energy difference between the initial state and the final state decreases at lower dihedral angles as shown in Fig. 2. The authors suppose that a linear relationship can be observed at lower dihedral angle, because the particle keeps its spherical shape approximately during sintering.

4. Summary

Pore channel closure is an essential process, which characterizes the beginning of the second stage of sintering. The sintering of a ring of three spheres is the simplest model for analyzing the pore channel closure, and the three-dimensional numerical simulation has been conducted by using Brakke's Surface Evolver program assuming an idealized sintering mechanism to avoid complications. The ring has a hole in the center. As the circular grain boundary expands in the initial stage of sintering, the hole radius shrinks, then, a triple junction is formed after the hole closure. The position of the mass center of a particle shifted during sintering, then, the shrinkage rate could be calculated from the motion of mass center. The force acting between particles,

that was the sintering force, was defined by including both surface tension and grain boundary tension. The shrinkage rate was approximately proportional to the sintering force, but became non-linear at lower γ_{gb}/γ_s. The sintering force, and also, shrinkage rate increased with decreasing γ_{gb}/γ_s, then, the hole closed in a short time at low γ_{gb}/γ_s.

References

1. Philibert, J., *Atom Movements, Diffusion and Mass Transport in Solid*. Les Editions de Physique, France, 1991.
2. Frenkel, J., Viscous flow of crystalline bodies under the action of surface tension. *J. Phys.*, 1945, **9**, 385–391.
3. Kuczynski, G. C., Self-diffusion in sintering of metallic particles. *Trans. Am. Inst. Mining. Met. Eng.*, 1949, **185**, 169–178.
4. Coble, R. L., Sintering crystalline solids. I. Intermediate and final state diffusion models. *J. Appl. Phys.*, 1961, **32**, 787–792.
5. Swinkels, F. R. and Ashby, M. F., A second report on sintering diagrams. *Acta Metall.*, 1981, **29**, 259–281.
6. Zeng, P., Zajac, S., Clapp, P. C. and Rifkin, J. A., Nanoparticle sintering simulations. *Mater. Sci. Eng. A*, 1998, **252**, 301–306.
7. Tikare, V., Braginsky, M. and Olevsky, E. A., Numerical simulation of solid-state sintering. I. Sintering of three particles. *J. Am. Ceram. Soc.*, 2003, **86**, 49–53.
8. Van de Vorst, G. A. L., Integral method for a two-dimensional Stokes flow with shrinking holes applied to viscous sintering. *J. Fluid Mech.*, 1993, **257**, 667–689.
9. Nichols, F. A. and Mullins, W. W., Surface- (interface-) and volume-diffusion contributions to morphological changes driven by capillarity. *Trans. AIME*, 1965, **233**, 1840–1848.
10. Glaeser, A. M., Model studies of Rayleigh instabilities via microdesigned interfaces. *Interf. Sci.*, 2001, **9**, 65–82.
11. Exner, H. E., Principles of single phase sintering. *Rev. Powd. Met. Phys. Ceram.*, 1979, **1**, 7–251.
12. Kellett, B. J. and Lange, F. F., Thermodynamics of densification I: sintering of simple particle arrays, equilibrium configurations, pore stability, and shrinkage. *J. Am. Ceram. Soc.*, 1989, **72**, 725–734.
13. Zhou, H. and Derby, J. J., An assessment of a parallel, finite element method for three-dimensional, moving-boundary flows driven by capillarity for simulation of viscous sintering. *Int. J. Numer. Meth. Fluids*, 2001, **36**, 841–865.
14. Maximenko, A., Roebben, G. and Van der Biest, O., Modeling of non-linear phenomena during deformation of interparticle necks by diffusion-controlled creep. *Acta Mater.*, 2002, **50**, 3651–3659.
15. Wakai, F. and Aldinger, F., Equilibrium configuration of particles in sintering under constraint. *Acta Mater.*, 2003, **51**, 641–652.
16. Wakai, F. and Aldinger, F., Sintering through surface motion by the difference in mean curvature. *Acta Mater.*, 2003, **51**, 4013–4024.
17. Wakai, F., Modeling and simulation of elementary processes in ideal sintering. *J. Am. Ceram. Soc.*, 2006, **89**, 1471–1484.
18. Brakke, K. A., The Surface Evolver. *Exp. Math.*, 1992, **1**, 141–165.
19. Wakai, F., Enomoto, N. and Ogawa, H., Three-dimensional microstructural evolution in ideal grain growth–general statistics. *Acta Mater.*, 2000, **48**, 1297–1311.
20. Wakai, F., Yoshida, M., Shinoda, Y. and Akatsu, T., Coarsening and grain growth in sintering of two particles of different sizes. *Acta Mater.*, 2005, **53**, 1361–1371.
21. Johnson, D. L., New method of obtaining volume, grain-boundary, and surface diffusion coefficients from sintering data. *J. Appl. Phys.*, 1969, **40**, 192–200.
22. Gregg, R. A. and Rhines, F. N., Surface tension and the sintering force in copper. *Metall. Trans.*, 1973, **4**, 1365–1374.
23. Beere, W., The second stage sintering kinetics of powder compacts. *Acta Metall.*, 1975, **23**, 139–145.
24. Jagota, A. and Dawson, P. R., Micromechanical modeling of powder compacts. I. Unit problems for sintering and traction induced deformation. *Acta Metall.*, 1988, **36**, 2551–2561.
25. Bordia, R. K. and Scherer, G. W., On constrained sintering. I. Constitutive model for a sintering body. *Acta Metall.*, 1988, **36**, 2393–2397.
26. McMeeking, R. M. and Kuhn, L. T., A diffusional creep law for powder compacts. *Acta Metall. Mater.*, 1992, **40**, 961–969.